A novel SPH-SIMSAND based approach for modelling of granular collapse

Zhen-Yu YIN[a,b,*], Zhuang JIN[a], Panagiotis KOTRONIS[a] and Ze-Xiang WU[a]

Affiliations:

[a] Research Institute of Civil Engineering and Mechanics (GeM), UMR CNRS 6183, Ecole Centrale de Nantes, Nantes 44321, France

[b] Key Laboratory of Geotechnical and Underground Engineering of Ministry of Education, Department of Geotechnical Engineering, Tongji University, Shanghai 200092, China

* Corresponding author: Dr. Zhen-Yu YIN, Email: zhenyu.yin@gmail.com; Tel: +33 (0)2 40 37 15 88 / Fax: +33 (0)2 40 37 25 35

Abstract: Granular collapse is a common issue in natural hazards. This paper proposes a novel numerical approach on modelling granular column collapse. A newly developed critical state based constitutive model SIMSAND is adopted to combine with the Smoothed Particle Hydrodynamics (SPH) method for reproducing realistically the large deformation during collapse. Rectangular channel and two-dimensional column tests are first simulated for the validation. The effects of aspect ratio and initial soil density are further investigated by additional simulations. It is demonstrated that the novel SPH-SIMSAND approach is helpful to improve the understanding of granular collapse and should be an effective computational tool for the analysis of real scale granular flow.

Keywords: Granular material; collapse; SPH; large deformation analysis; granular flow; critical state

1 Introduction

Granular collapse, such as debris, rock avalanches and landslides is a common issue in natural hazards. In order to understand this phenomenon, two types of experiments were performed: rectangular channel flowing tests (Balmforth and Kerswell 2005; Lajeunesse et al. 2005; Lube et al. 2005; Lube et al. 2007; Bui et al. 2008; Crosta et al. 2009) and column flowing tests Lube et al. (2004, 2005 and 2007). In the first, granular collapse is obtained by putting the granular material in a rectangular channel and quickly removing a vertical side boundary, while in the second the granular material is in a hollow cylinder pipe.

Daerr and Douady (1999) presented that the final deposit morphology for the column collapse tests depends on the initial soil density based on only a low aspect ratio test. Later on, experimental results by others (Lajeunesse et al. 2004; Lube et al. 2004; Lube et al. 2005; Lube et al. 2007) showed that the final deposit morphology (deposit radius, deposit height and slumping velocity) mainly depends on the initial aspect ratio of the granular column without showing the influence of soil density. More recently, various numerical studies were also conducted to investigate the granular collapse using the physics based Discrete Element Method (DEM). The results also showed that the final deposit morphology depends on the initial aspect ratio (Staron and Hinch 2005; Zenit 2005; Lacaze et al. 2008; Girolami et al. 2012; Soundararajan 2015; Utili et al. 2015). In these studies, the effect of the initial void ratio (corresponding to the soil density) was again ignored. To replenish this, Kermani et al. (2015) and Soundararajan (2015) simulated the effect of initial porosity on the 3D asymmetrical collapsing considering different aspect ratios. However, the number of particles in the majority of DEM simulations is limited and far from a real physical model or case due to computational efficiency issues. The applicability of the DEM method to a real scale problem is thus still questionable.

Finite element method is a powerful way to simulate problems in geotechnics (Shen et al. 2014; Shen et al. 2017; Wu et al. 2016; Wu et al. 2017a). The method was also applied to analyse granular column collapse using Mohr-Coulomb and Drucker-Prager constitutive models and the Arbitrary Lagrangian-Eulerian (ALE) technique (Crosta et al. 2009), the Particle Finite Element Method (PFEM) (Zhang et al. 2015), the Smooth Particle Hydrodynamics (SPH) method (Bui et al. 2008; Nguyen et al. 2016) and the Material Point Method (MPM) (Sołowski and Sloan 2015). However, these adopted constitutive models adopted up to now are not ~~appreciated~~ appropriate to describe the state-dependent behaviour of soils. Since the constitutive model is a key component controlling the physics of finite element analysis, the well accepted critical state modelling theory for granular material should be considered.

In this paper, a critical state based model accounting for soil density effects is first adopted and implemented into to combine with the Smoothed Particle ~~Method~~ Hydrodynamics (SPH) ~~technique~~ method technique for large deformation analysis. Then, rectangular channel soil collapse tests are simulated and the combined numerical tool is validated. Granular column collapse tests with different aspect ratios are simulated for further validation in terms of the final deposit morphologies, the dynamical flowing profiles and the undisturbed areas. Finally, additional simulations for different initial void ratios (e_0 =0.75, 0.85, 0.95 and 1.05) are conducted to investigate the effect of soil density on the final deposit morphology. The collapse evolution process is monitored and the ability of the adopted modelling strategy to reproduce the influences of the initial aspect ratio and the soil density is evaluated.

2 Numerical methods and constitutive model for simulation

2.1 SPH method

The SPH method implemented in the finite element code ABAQUS/Explicit was adopted in this study to solve large deformation problems. The method was first developed by Gingold and Monaghan (1977) for simulations in astrophysics. Further developments allowed for applications to a broad range of problems in solid mechanics. In SPH simulations, the computational domain is discretized into a finite number of particles, each representing a certain volume and mass of material (fluid or solid) and carrying simulation parameters such as acceleration, velocity, density and pressure/stress, shown in Figure 1(a).

The material properties $f(x)$ at any point x in the simulation domain are then calculated according to an interpolation process over its neighbouring particles that are within an influence domain Ω through

$$f(x) = \int_{\Omega} f(x') W(x' - x, h) \tag{1}$$

where W is the kernel or smoothing function, which is essentially a weighting function. This continuous integral representation of the field variable $f(x)$ can be further approximated by the summation over neighbouring particles as

$$f(x) = \sum_{i=1}^{N} f(x_i) W(x - x_i, h) V_i = \sum_{i=1}^{N} f(x_i) W(x - x_i, h) \frac{m_i}{\rho_i} \tag{2}$$

where V_i, m_i and ρ_i are the volume, mass and density of the particle i respectively and N is the number of particles within the influence domain. The spatial derivative of the field variable $f(x)$ can be approximated through the differential operations on the kernel function

$$\frac{\partial f(x)}{\partial x} = \sum_{i=1}^{N} \frac{m_i}{\rho_i} f(x_i) \frac{\partial W(x - x_i, h)}{\partial x_i} \tag{3}$$

The efficiency and accuracy of SPH simulations depend on the kernel function. The SPH

particles are used as interpolation points and are the basis for calculating all the field variables in the continuum. Like the objects in astrophysics, the SPH particles can be separated by a large distance. The field variables between the SPH particles are approximated (smoothed) by smoothing shape functions. The interaction between the SPH particles starts when a particle gets to a certain distance (smoothing length h) from another one. SPH particles interact with each other only if they are within the influence domain. Otherwise, they are independent from each other. Therefore, a larger smoothing length (i.e. larger influence domain) generally results in a smoother or more continuous behaviour as the SPH particles are more interdependent. Whereas, a smaller smoothing length (i.e. smaller influence domain) generally yields more discrete behaviours as the SPH particles are more independent.

A major advantage of the SPH method is that there is no need for a fixed computational grid when calculating spatial derivatives. Instead, estimates of derivatives are obtained from analytical expressions based on the derivatives of the smoothing functions (Li and Liu 2002). Since the connectivity between the particles is generated as a part of the computation and can change over the time, the SPH method can handle very large deformations and displacements.

2.2 Explicit finite element method

The SPH method implemented in ABAQUS uses the explicit time integration method (Hibbitt et al. 2001). As shown in Figure 1(b), the equilibrium condition is first written with the balance of internal force and external force,

$$M\ddot{u}_{(t)} = P_{(t)} - I_{(t)} \tag{4}$$

where M is the mass matrix; $\ddot{u}$ is the acceleration; P is the applied external force vector, and I is the internal force vector.

The equations of motion for the body are then integrated using the explicit time central-difference integration rule as follows:

$$\begin{cases} \dot{u}_{\left(t+\frac{\Delta t}{2}\right)} = \dot{u}_{\left(t-\frac{\Delta t}{2}\right)} + \dfrac{\Delta t_{(t+\Delta t)} + \Delta t_{(t)}}{2} \ddot{u}_{(t)} \\ u_{(t+\Delta t)} = u_{(t)} + \Delta t_{(t+\Delta t)} \dot{u}_{\left(t+\frac{\Delta t}{2}\right)} \end{cases} \tag{5}$$

where u is the displacement and the subscript t refers to the time in an explicit dynamic step. $\dot{u}$ is the velocity; Δt is the increment of time. For the stability of calculation, the time increment Δt should be smaller than a limited value $\Delta t \approx L_{\min}/c_d$ with the smallest element dimension of mesh L_{min} and the dilatory wave speed c^d.

Finally, incremental strain calculated by incremental displacement will be called by the constitutive model to update stresses and then internal forces, up to a new equilibrium condition.

2.3 Adopted critical state based model SIMSAND

The SIMSAND model was developed based on the Mohr-Coulomb model by implementing the critical state concept (Yin et al. 2016a; Jin et al. 2017) with non-linear elasticity, non-linear plastic hardening, and a simplified three-dimensional strength criterion. The state-dependent peak strength and stress-dilatancy (contraction or dilation) are well captured by the SIMSAND model (Jin et al. 2017). The basic constitutive equations are summarized in Table 1. The model parameters with their definitions are summarized in Table 2. The calibration of the model parameters can be carried out using a straightforward way (Wu et al. 2017b) or using optimisation methods (Jin et al. 2016a,b; Yin et al. 2016b).

The adopted SIMSAND model was implemented into ABAQUS/Explicit as a user-defined material model via user material subroutine VUMAT. The procedure of model implementation follows the way of Hibbitt et al. (2001). In ABAQUS/Explicit combining with VUMAT, the strain

increment on the element $\Delta\varepsilon$ at Δt is first solved by ABAQUS using the presented explicit time central-differential integration method. Then, the stress increment $\Delta\sigma$ is updated through VUMAT using the solved $\Delta\varepsilon$. For the stress integration, the cutting plane algorithm proposed by Ortiz and Simo (1986) was adopted. The implementation of finite element method was then verified by simulating above mentioned drained triaxial tests before modelling the granular collapse.

3 Rectangular channel soil collapse simulations

3.1 Experimental and numerical simulation configurations

In order to validate the SIMSAND model and the adopted numerical integration scheme, the rectangular channel soil collapse tests (Bui et al. 2008) were simulated hereafter. In experiments small aluminium bars of various diameters (0.1cm and 0.15cm) were used to model the soil. The bars were initially arranged into an area of ~~200 mm~~ 20cm length × ~~100 mm~~ 10cm height × ~~20 mm~~ 2cm width, delimited by two flat solid walls. The experiment starts by quickly moving the right wall horizontally to the right causing the flow of the aluminium bars to the side due to gravity (Figure 2).

In the numerical model, the spatial discretization domain is shown in Figure 3(a). SPH particles are used to model the soil while the two solid walls are discretized with rigid hexahedral finite elements. The initial SPH particles distance is (approximately) the same in the horizontal and vertical directions, in order to reproduce homogenous conditions.

A cell size of ~~2 mm~~ 0.2cm was estimated by checking mesh-dependency (see Figure. 3(c-d)) so that the particle space or the particle diameter is one-half of the cell size (eight particles in each cell). The total number of the particle is 400000. The bottom surface was set as fixed boundary while symmetrical conditions were assumed for the four lateral boundaries.

The simulation was carried out in two steps: to balance the geostatic field and to move the right wall along the horizontal direction with a speed of 1m/s to the right. The contacts between the sand and walls were described by the classical Coulomb friction law with a friction coefficient $\mu = \tan(\phi_\mu/2) = 0.28$.

Following Lube et al.(2004 and 2005), the collapse behaviour is less sensitive to the grain properties of granular material comparing to the density. Meanwhile, lack of mechanical tests on used material, the model parameters of Toyoura sand were adopted for simulations. Figure 4 presents the typical state-dependent behaviour of granular materials simulated by the model under a very low confining stress as the condition in experiments. As shown in this figure, the initial void ratio (or initial density) influences significantly the peak strength and the dilation/contraction of granular material, which should be considered in granular collapse since the density is highly changing during the collapse.

3.2 Numerical validation

Different void ratios from 0.75 to 1.05 were assumed for simulations and compared with experimental results. As shown in Figure 5, higher the initial density (or smaller the void ratio) is, stiffer the free surface and failure line, and longer the run-out distance is. This agrees with the experimental results of Lube et al. (2005). Luckily, the simulation with e_0= 0.95 fits well the experiment. Thus, the e_0= 0.95 was adopted as a reference void ratio for the following sections.

During the simulation using the SPH method, each particle represents one gauss integration point. Accordingly, similarly to the element in FEM, the total strain of each particle is divided into the elastic and plastic strains when using the SIMSAND-model in SPH. In this study, the equivalent plastic strain is defined as $\sqrt{2/3\left(\dot{e}_{ij}^{p}:\dot{e}_{ij}^{p}\right)}$ (where $\dot{e}_{ij}^{p}$ is tensor of deviatoric plastic strain rate) was

used to describe the plastic deformation. Figure 6 shows the calculated deformed column with the distribution of deviatoric plastic strain at different time steps. The movement takes place for approximately 0.6s.

4 Influence of aspect ratio

4.1 Numerical simulation configurations

In order to have a further understanding on the granular column collapse, the two-dimensional column collapse with different initial aspect ratio was simulated.

In the numerical model, the spatial discretization domain has the same dimensions as in the experiments of Lube et al. (2005) shown in Figure 7, where h_i is the initial height, d_i the initial basal length and $a=h_i/d_i$ the aspect ratio of the granular column. As in the experiments, six aspect ratios were studied (a=0.5, 1.0, 1.5, 3.0, 7.0, 9.0) in which the column initial basal length is taken constant and equal to 10 cm. The element size for all aspect ratios are ~~2 mm~~ 0.2cm, using which a total of elements from 31250 to 562500 (PC3D) are discretized for different aspect ratios of columns, summarized in Table 3.

4.2 Comparisons and discussions

Three different aspect ratios (a = 0.5, 1. 5 and 7.0) in the numerical results are compared with the experimental results of Lube et al. (2005) in Figure 8, where the gradually varied color represents the distribution of the deviatoric plastic strain. A good agreement is observed in terms of deposit morphology. Furthermore, simulations captured the progressive collapsing process, more specifically:

(1) For a = 0.5: the outer region at the bottom flows and the length of the run-out region at the column foot increases. The inner region is less disturbed than other cases and a flat area remains at the top.

(2) For a = 1.5: the run-out distance at the bottom increases and a flat undisturbed area is created at the top during the initial stage. A cone tip is formed at the end.

(3) For a = 7.0: an important degradation of the column height first happens. Then, the run-out distance at the column foot increases and the upper initially undisturbed surface begins to flow. Finally, a very large run-out distance with a cone tip is formed.

4.3 Flow description

Figure 9 shows the successive numerical granular collapse profiles for the three aspect ratios. Lube et al. (2004) summarised three deposit morphologies based on the aspect ratio range: (1) a <0.74, (2) 0.74 < a <1.7 and (3) a >1.7. These distinctive flow processes are well captured by simulations:

(1) For a=0.5 (< 0.74): a lateral flow develops at the column foot and a flat undisturbed area remains at the top. The deposit height h_0 stays constant.

(2) For 0.74 < a=1.5 <1.7: the evolution of the lateral flow is accompanied by a small decrease of the initial height h_0. A wedge shape is formed at the end.

(3) For a =7 >1.7: initially, the column height greatly decreases but the upper surface remains unchanged. Then, the lateral flow develops quickly. Simultaneously, the length of the upper surface decreases and forms a dome-like shape. At the final stage, the run-out distance d_∞ is important and a wedge shape is formed at the top h_∞.

Figure 10 shows the comparison of plastic strain fields between simulations with different aspect ratios, where the smallest value of deviatoric plastic strain ε_d^p is coloured in black, and the undisturbed stable area inside the granular column is suggested by a relatively small value of deviatoric plastic strain. Then, it can be found that only for the cases of small aspect ratios a = 0.5, 1.0 and 1.5, an undisturbed trapezoid area develops on the upper free surface of the column as colouring with the highlighted black. But for the cases of large aspect ratios a = 3.0, 7.0 and 9.0, the upper free surface develops a triangle area and the repose angle presents an increasing trend.

5 Influence of soil density

5.1 Deposit morphology

In order to study the influence of soil density, granular columns with four initial void ratios (e_0 = 0.75, 0.85, 0.95 and 1.05, corresponding to a unit weight of γ = 1.51, 1.43, 1.36 and 1.29 when G_s=2.65) and for six aspect ratios (a = 0.5, 1.0, 1.5, 3.0, 7.0 and 9.0) were simulated hereafter. The numerical results are compared with the best-fitting equations shown in Figure 11. It can be found that, the numerical results are in agreement with the best-fitting equations of Lube et al. (2005) for the normalized final run-out distance when e_0=0.95. Difference however appears for smaller initial void ratios, especially in the cases of larger aspect ratios. The normalized final deposit height seems less sensitive to the soil density. However, the effect increases for the cases of higher aspect ratios. All comparisons indicate that the deposit morphology (final run-out distance and final deposit height) depends on not only the aspect ratio but also the initial density. This is also in agreement with results by Discrete Element Method (Kermani et al. 2015).

Figure 12 presents the final deposit morphology of the simulations with different initial void ratios. It can be found that the final deposit morphology is sensitive to the initial void ratio or soil

density. For the cases of lower column a < 1.15, the height of the circular undisturbed zone in the upper surface is maintained in the same. But its area is decreased. The run-out distance increases with the ~~increasing~~ increase of the initial void ratio (or ~~decreasing~~ decrease of initial soil density). For the cases of the higher column a > 1.15, the denser granular material causes shorter run-out distance and higher final deposited height in agreement with the DEM simulations by Kermani et al. (2015) and experiments by Daerr and Douady (1999). It illustrates that the influence of void ratio or soil density on granular collapse was well captured by using SPH technique with the critical state based SIMSAND model. The difference of deposit morphology between different void ratios for the same aspect ratio can be explained by the stress-dilatancy of granular soils. For dense sand, a stronger interlocking force between particle is developing with a higher mobilized strength and finally forms a stable inner region during the stage of collapsing. Therefore, a denser granular column corresponds to a bigger inclination of the slope surface with a higher deposit height and smaller run-out distance.

5.2 Monitoring collapse

The collapsing time t was normalised by the intrinsic critical time t_c used for the dimensionless analysis where the value of t_c can be calculated by the initial height of sand column $t_c = \sqrt{h_i/g}$ (Soundararajan 2015). Figures 13 and 14 present the simulation results of the normalized run-out distance $(d_\infty - d_i)/d_i$ and the normalized deposit height h_∞/d_i with the normalized time t/t_c. All results present an ‘‘S-shape’’ curve with two successive stages, regardless the initial aspect ratios and void ratios. First an acceleration and then a deceleration stage starting close to $1.5t_c \sim 2.0t_c$. Collapse ceases approximately at $3.5t_c$.

The following conclusions can also be made:

(1) For the same initial void ratio, a higher aspect ratio leads to a more important normalized run-out distance and deposit height.

(2) For the same aspect ratio, denser sand (smaller initial void ratio) leads to a more important deposit height but to a shorter run-out distance in the same time scale.

(3) The normalized deposit height initially increases when the right boundary plate is lifted (Figure. 14(a-c)). This uplift depends strongly on the soil density. A denser soil leads to a more important uplift. The reason for this is again the density effect, which develops more on denser sand due to the stronger interlocking between particles at initial shearing.

6 Conclusion

A numerical investigation on granular collapse, based on the critical state soil model SIMSAND and the SPH method has been carried out. The validation was first provided with comparing experimental data from rectangular channel and two-dimensional column collapse tests. Then, the influence of the initial aspect ratio and the soil density was studied in details.

All comparisons show that the adopted numerical strategy is able to reproduce qualitatively and quantitatively the main behaviours of granular column collapse, i.e. free surface, failure line, final deformed profile for the rectangular channel test, final run-out distance and deposit height. More specifically, when the initial soil density decreases the failure surface shrinks and free surface enlarges. A lower initial void ratio generates a stronger interlocking force leading to a higher deposit height and a shorter run-out distance.

The combination of the SIMSAND model with the SPH method is able to reproduce granular collapse taking into account the influence of different aspect ratios and soil densities. Therefore, It provides an effective computational tool for the analysis of real scale granular flow.

Acknowledgements

The financial support for this research came from the National Natural Science Foundation of China (Grant Nos. 41372285, 51579179), and the Region Pays de la Loire of France (project RI-ADAPTCLIM).

References

Balmforth, N., and Kerswell, R. (2005). "Granular collapse in two dimensions." *Journal of Fluid Mechanics*, 538, 399-428.

Bui, H. H., Fukagawa, R., Sako, K., and Ohno, S. (2008). "Lagrangian meshfree particles method (SPH) for large deformation and failure flows of geomaterial using elastic–plastic soil constitutive model." *International Journal for Numerical and Analytical Methods in Geomechanics*, 32(12), 1537-1570.

Crosta, G., Imposimato, S., and Roddeman, D. (2009). "Numerical modeling of 2‐D granular step collapse on erodible and nonerodible surface." *Journal of Geophysical Research: Earth Surface*, 114(F3).

Daerr, A., and Douady, S. (1999). "Sensitivity of granular surface flows to preparation." *EPL (Europhysics Letters)*, 47(3), 324-330.

Gingold, R. A., and Monaghan, J. J. (1977). "Smoothed particle hydrodynamics: theory and application to non-spherical stars." *Monthly notices of the royal astronomical society*, 181(3), 375-389.

Girolami, L., Hergault, V., Vinay, G., and Wachs, A. (2012). "A three-dimensional discrete-grain model for the simulation of dam-break rectangular collapses: comparison between numerical results and experiments." *Granular Matter*, 14(3), 381-392.

Hibbitt, Karlsson, and Sorensen (2001). *ABAQUS/Explicit: User's Manual*, Hibbitt, Karlsson and Sorenson Incorporated.

Jin, Y.-F., Wu, Z.-X., Yin, Z.-Y., and Shen, J. S. (2017). "Estimation of critical state-related formula in advanced constitutive modeling of granular material." *Acta Geotechnica*, 1-23.

Jin, Y.-F., Yin, Z.-Y., Shen, S.-L., and Hicher, P.-Y. (2016a). "Investigation into MOGA for

identifying parameters of a critical-state-based sand model and parameters correlation by factor analysis." *Acta Geotechnica*, 11(5), 1131-1145.

Jin, Y. F., Yin, Z. Y., Shen, S. L., and Hicher, P. Y. (2016b). "Selection of sand models and identification of parameters using an enhanced genetic algorithm." *International Journal for Numerical and Analytical Methods in Geomechanics*, 40(8), 1219-1240.

Kermani, E., Qiu, T., and Li, T. (2015). "Simulation of collapse of granular columns using the discrete element method." *International Journal of Geomechanics*, 15(6), ~~04015004~~ doi:10.1061/(ASCE)GM.1943-5622.0000467.

Lacaze, L., Phillips, J. C., and Kerswell, R. R. (2008). "Planar collapse of a granular column: Experiments and discrete element simulations." *Physics of Fluids*, 20(6), ~~063302~~ doi: doi/abs/10.1063/1.2929375.

Lajeunesse, E., Mangeney-Castelnau, A., and Vilotte, J. (2004). "Spreading of a granular mass on a horizontal plane." *Physics of Fluids*, 16(7), 2371-2381.

Lajeunesse, E., Monnier, J., and Homsy, G. (2005). "Granular slumping on a horizontal surface." *Physics of fluids*, 17(10), ~~103302~~ doi: 10.1063/1.2087687.

Li, S., and Liu, W. K. (2002). "Meshfree and particle methods and their applications." *Applied Mechanics Reviews*, 55(1), 1-34.

Lube, G., Huppert, H. E., Sparks, R. S. J., and Freundt, A. (2005). "Collapses of two-dimensional granular columns." *Physical Review E*, 72(4), ~~041301~~ doi: 10.1061/(ASCE)GM.1943-5622.0000467.

Lube, G., Huppert, H. E., Sparks, R. S. J., and Freundt, A. (2007). "Static and flowing regions in granular collapses down channels." *Physics of Fluids*, 19(4), ~~043301~~ doi: 10.1063/1.2712431.

Lube, G., Huppert, H. E., Sparks, R. S. J., and Hallworth, M. A. (2004). "Axisymmetric collapses

of granular columns." *Journal of Fluid Mechanics*, 508, 175-199.

Nguyen, C. T., Nguyen, C. T., Bui, H. H., Nguyen, G. D., and Fukagawa, R. (2016). "A new SPH-based approach to simulation of granular flows using viscous damping and stress regularisation." *Landslides*, 1-13.

Ortiz, M., and Simo, J. (1986). "An analysis of a new class of integration algorithms for elastoplastic constitutive relations." *International Journal for Numerical Methods in Engineering*, 23(3), 353-366.

Shen, S.-L., Wu, H.-N., Cui, Y.-J., and Yin, Z.-Y. (2014). "Long-term settlement behaviour of metro tunnels in the soft deposits of Shanghai." *Tunnelling and Underground Space Technology*, 40, 309-323.

Shen, S.-L., Wu, Y.-X., and Misra, A. (2017). "Calculation of head difference at two sides of a cut-off barrier during excavation dewatering." *Computers and Geotechnics*, 91, 192-202.

Sheng, D., Sloan, S., and Yu, H. (2000). "Aspects of finite element implementation of critical state models." *Computational mechanics*, 26(2), 185-196.

Sołowski, W., and Sloan, S. (2015). "Evaluation of material point method for use in geotechnics." *International Journal for Numerical and Analytical Methods in Geomechanics*, 39(7), 685-701.

Soundararajan, K. K. (2015). "Multi-scale multiphase modelling of granular flows." University of Cambridge.

Staron, L., and Hinch, E. (2005). "Study of the collapse of granular columns using two-dimensional discrete-grain simulation." *Journal of Fluid Mechanics*, 545, 1-27.

Utili, S., Zhao, T., and Houlsby, G. (2015). "3D DEM investigation of granular column collapse: evaluation of debris motion and its destructive power." *Engineering geology*, 186, 3-16.

Wu, Y.-X., Shen, J. S., Chen, W.-C., and Hino, T. (2017a). "Semi-analytical solution to pumping

test data with barrier, wellbore storage, and partial penetration effects." *Engineering Geology*.

Wu, Y.-X., Shen, S.-L., and Yuan, D.-J. (2016). "Characteristics of dewatering induced drawdown curve under blocking effect of retaining wall in aquifer." *Journal of Hydrology*, 539, 554-566.

Wu, Z.-X., Yin, Z.-Y., Jin, Y.-F., and Geng, X.-Y. (2017b). "A straightforward procedure of parameters determination for sand: a bridge from critical state based constitutive modelling to finite element analysis." *European Journal of Environmental and Civil Engineering*, 1-23.

Yao, Y., Hou, W., and Zhou, A. (2009). "UH model: three-dimensional unified hardening model for overconsolidated clays." *Geotechnique*, 59(5), 451-469.

Yao, Y., Lu, D., Zhou, A., and Zou, B. (2004). "Generalized non-linear strength theory and transformed stress space." *Science in China Series E: Technological Sciences*, 47(6), 691-709.

Yao, Y., Sun, D., and Matsuoka, H. (2008). "A unified constitutive model for both clay and sand with hardening parameter independent on stress path." *Computers and Geotechnics*, 35(2), 210-222.

Yin, Z.-Y., Chang, C. S., and Hicher, P.-Y. (2010). "Micromechanical modelling for effect of inherent anisotropy on cyclic behaviour of sand." International Journal of Solids and Structures, 47(14), 1933-1951.

Yin, Z. Y., and Chang, C. S. (2013). "Stress–dilatancy behavior for sand under loading and unloading conditions." International Journal for Numerical and Analytical Methods in Geomechanics, 37(8), 855-870.

Yin, Z.-Y., Hicher, P.-Y., Dano, C., and Jin, Y.-F. (2016a). "Modeling mechanical behavior of very

coarse granular materials." *Journal of Engineering Mechanics*, 143(1), ~~C4016006~~ doi:10.1061/(ASCE)EM.1943-7889.0001059.

Yin, Z.-Y., Jin, Y.-F., Shen, S.-L., and Huang, H.-W. (2016b). "An efficient optimization method for identifying parameters of soft structured clay by an enhanced genetic algorithm and elastic–viscoplastic model." *Acta Geotechnica*, 1-19.

Zenit, R. (2005). "Computer simulations of the collapse of a granular column." *Physics of Fluids*, 17(3), ~~031703~~ doi: 10.1063/1.1862240.

Zhang, X., Krabbenhoft, K., Sheng, D., and Li, W. (2015). "Numerical simulation of a flow-like landslide using the particle finite element method." *Computational Mechanics*, 55(1), 167-177.

Table

Table 1 Basic constitutive equations of SIMSAND model

Components	Constitutive equations
Elasticity	$\dot{\varepsilon}_{ij}^{e}=\frac{1+\upsilon}{3K\left(1-2\upsilon\right)}\sigma'_{ij}-\frac{\upsilon}{3K\left(1-2\upsilon\right)}\sigma'_{kk}\delta_{ij}\qquad K=K_0\cdot p_{at}\frac{\left(2.97-e\right)^2}{\left(1+e\right)}\left(\frac{p'}{p_{at}}\right)^{\zeta}$
Yield surface	$f=\frac{q}{p'}-H$
Potential surface	$\frac{\partial g}{\partial p'}=A_d\left(M_{pt}-\frac{q}{p'}\right);\ \frac{\partial g}{\partial s_{ij}}=\left\{1\quad 1\quad 1\quad 1\quad 1\quad 1\right\}$
Hardening rule	$H=\frac{M_p\varepsilon_d^p}{k_p+\varepsilon_d^p}$
Critical state with inter-locking effects	$e_c=e_{ref}-\lambda\left(\frac{p'}{p_{at}}\right)^{\xi}\qquad \tan\phi_p=\left(\frac{e_c}{e}\right)^{n_p}\tan\phi_\mu\qquad \tan\phi_{pt}=\left(\frac{e_c}{e}\right)^{-n_d}\tan\phi_\mu$
Three-dimensional strength criterion	$M_p=\frac{6\sin\phi_p}{3-\sin\phi_p}\left[\frac{2c_1^{\,4}}{1+c_1^{\,4}+\left(1-c_1^{\,4}\right)\sin 3\theta}\right]^{\frac{1}{4}}\quad \text{with } c_1=\frac{3-\sin\phi_p}{3+\sin\phi_p}$ $M_{pt}=\frac{6\sin\phi_{pt}}{3-\sin\phi_{pt}}\left[\frac{2c_2^{\,4}}{1+c_2^{\,4}+\left(1-c_2^{\,4}\right)\sin 3\theta}\right]^{\frac{1}{4}}\quad \text{with } c_2=\frac{3-\sin\phi_{pt}}{3+\sin\phi_{pt}}$

* p_{at} is the atmospheric pressure (p_{at} = 101.3 kPa); p' is effective mean pressure; q is the deviatoric stress; e_c is critical state void ratio;ϕ_p peak friction angle; ϕ_{pt} phase transformation friction angle; M_{pt} is stress ratio corresponding to the phase transformation; M_p is peak stress ratio; θ is lode's angle with its effect introduced by using Sheng et al. (2000) which is similar to Yao et al.(2004, 2008 and 2009); n_p and n_d are interlocking parameters controlling the degree of interlocking due to neighbouring particles according to Yin and Chang (2010, 2013).

Table 2 Parameters of SIMSAND model and values of parameters for Toyoura sand

Parameters	**Definitions**	**Value**
K_0	Referential bulk modulus (dimensionless)	130
υ	Poisson's ratio	0.2
n	Elastic constant controlling nonlinear stiffness	0.5
ϕ_μ	Critical state friction angle	31.5
e_{ref}	Initial critical state void ratio	0.977
λ	Constant controlling the nonlinearity of CSL	0.0596
ξ	Constant controlling the nonlinearity of CSL	0.365
A_{d}	Constant of magnitude of the stress-dilatancy	0.7
k_{p}	Plastic modulus related constant	0.0044
n_{p}	inter-locking related peak strength parameter	2.4
n_{d}	inter-locking related phase transformation parameter	2.9

Table 3 Discretization parameters for all simulations

Aspect ratio a	Initial basal length ~~di~~ d_i (cm)	Initial height ~~hi~~ h_i (cm)	Column size(cm^3)	~~N°~~ Number of SPH particles
0.5	10	5	10×5×5	31250
1.0	10	10	10×10×5	62500
1.5	10	15	10×15×5	93750
3.0	10	30	10×30×5	187500
7.0	10	70	10×70×5	437500
9.0	10	90	10×90×5	562500

Figure captions

Figure 1 SPH numerical method (a) deformation of Smoothed Particle Hydrodynamics method and (b) Flow chart of explicit analysis

Figure 2 Rectangular channel soil collapse experiments

Figure 3 SPH particle density and mesh-dependency: (a) 2D spatial domain discretization for SPH particles and rigid hexahedral finite elements, (b) element size of 0.1 cm (c) element size of 0.15 cm (d) element size of 0.2 cm

Figure 4 Simulated stress-strain behavior of conventional triaixal tests using parameters of Toyoura sand: (a) deviatoric stress versus axial strain, (b) void ratio versus axial strain, and (c) void ratio versus mean effective stress in demi-logarithmic scale

Figure 5 Simulation results of column collapse: (a) final free surfaces and failure lines for various initial void ratios e_0=0.75, 0.85, 0.95, 1.05, (b) final deformed column in experiment, and (c) final deformed column by simulation with e_0=0.95

Figure 6 Deformed shape and deviatoric plastic strain distribution of granular column at different time steps

Figure 7 Discretization domain plane views for six aspect ratios $\boldsymbol{a}$

Figure 8 Comparison of progressive granular collapse between simulations and experiments for different aspect ratios of (a) a = 0.5, (b) a = 1.5 and (c) a = 7.0

Figure 9 Numerical progressive column collapse profiles for different aspect ratios of (a) a = 0.5, (b) a = 1.5 and (c) a =7.0

Figure 10 Side view of plastic deviatoric strain after collapsing with different a: (a) a = 0.5, (b) a =1.0, (c) a = 1.5, (d) a = 3.0 , (e) a = 7.0 and (f) a = 9.0

Figure 11 Comparison between the numerical simulations and the best-fitting equations of Lube et al. (2005) for different aspect ratios and initial void ratios (a) normalized final runout distance and (b) normalized final deposit height

Figure 12 Influence of the initial void ratio on the final deposit morphology for (a) a = 0.5; (b) a = 1.0; (c) a = 1.5; (d) a = 3.0; (e) a =7.0; (f) a = 9.0

Figure 13 Evolution of the normalized runout distance for different aspect ratios and initial void ratios

Figure 14 Evolution of the normalized deposit height for different aspect ratios and initial void ratios

Figure 1

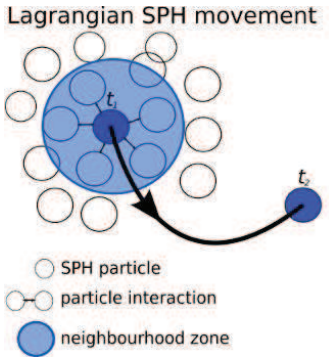
Lagrangian SPH movement
t_1
t_2
SPH particle
particle interaction
neighbourhood zone

(a)

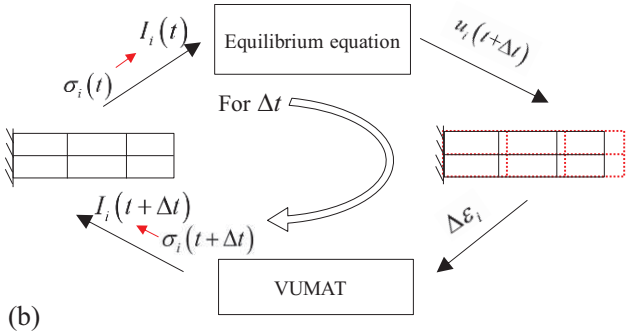
$I_i(t)$
$\sigma_i(t)$
Equilibrium equation
$u_i(t+\Delta t)$
For Δt
$I_i(t+\Delta t)$
$\sigma_i(t+\Delta t)$
$\Delta\varepsilon_i$
VUMAT

(b)

Figure 2

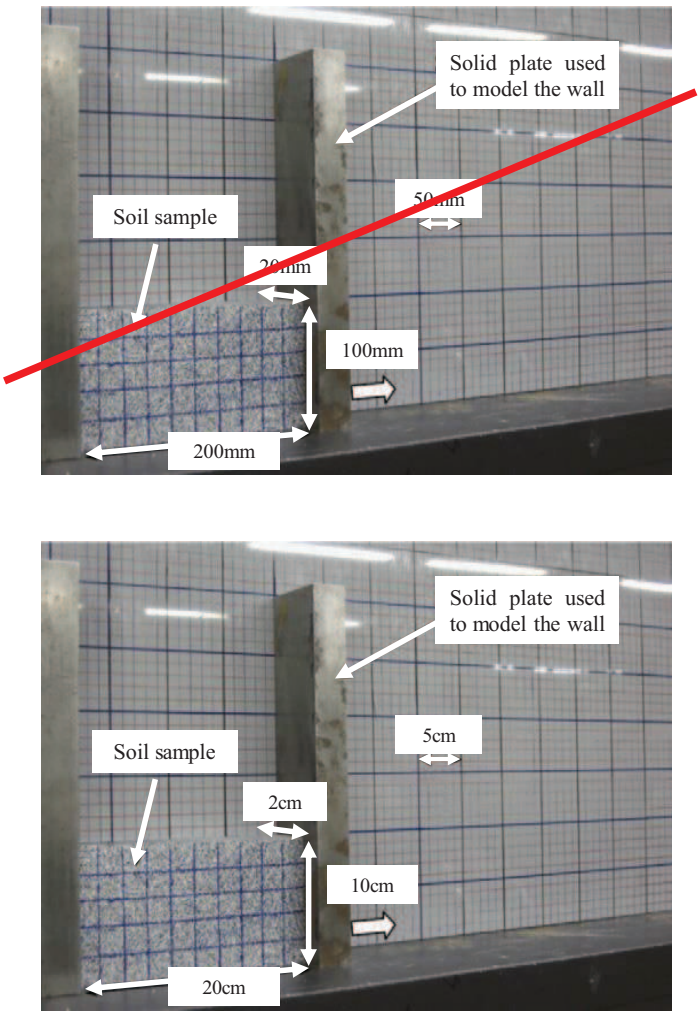
Solid plate used to model the wall
Soil sample
100mm
200mm
Solid plate used to model the wall
Soil sample
5cm
2cm
10cm
20cm

Figure 3

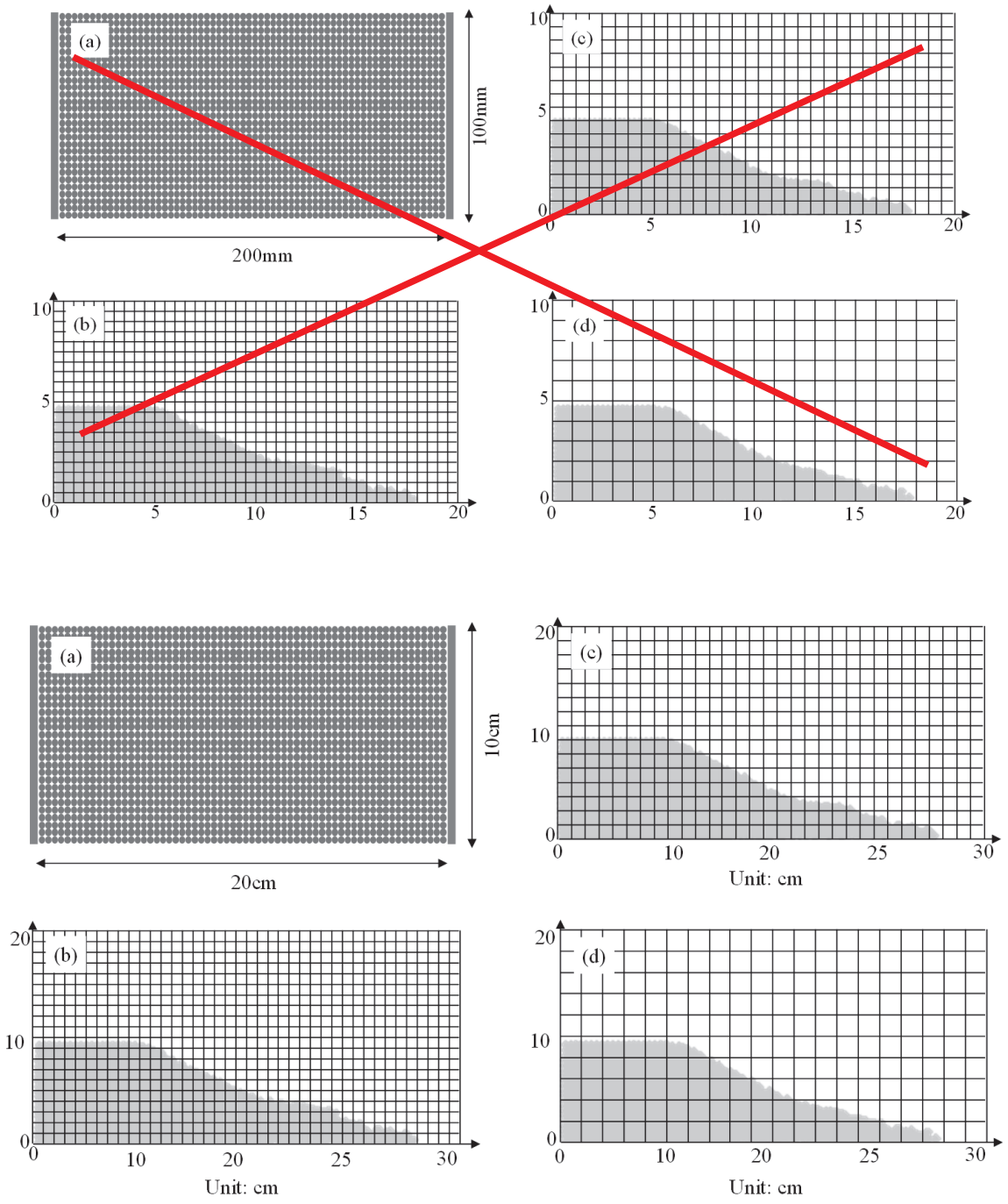
(a)
100mm
200mm
(c)
(b)
(d)
0
5
10
15
20
(a)
10cm
20cm
(c)
(b)
(d)
0
10
20
25
30
Unit: cm
Unit: cm
Unit: cm

Figure 4

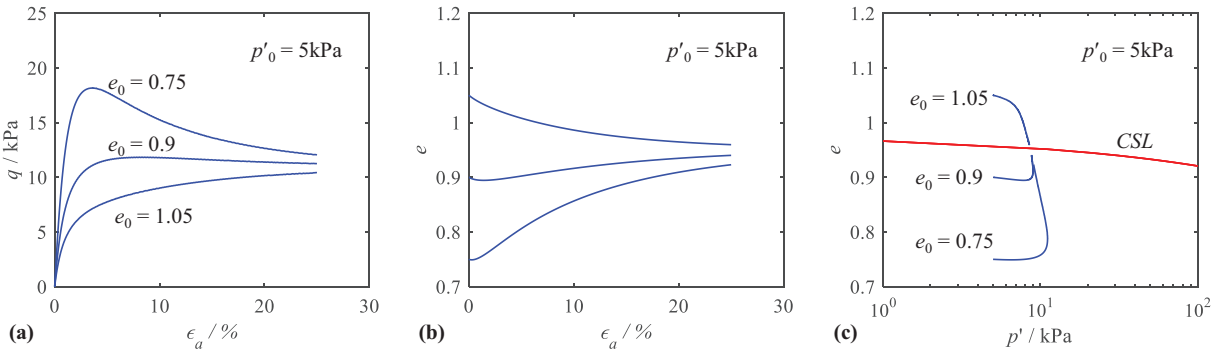
p'_0 = 5kPa
e_0 = 0.75
e_0 = 0.9
e_0 = 1.05
q / kPa
ϵ_a / %
(a)
p'_0 = 5kPa
e
ϵ_a / %
(b)
p'_0 = 5kPa
e_0 = 1.05
CSL
e_0 = 0.9
e_0 = 0.75
e
p' / kPa
(c)

Figure 5

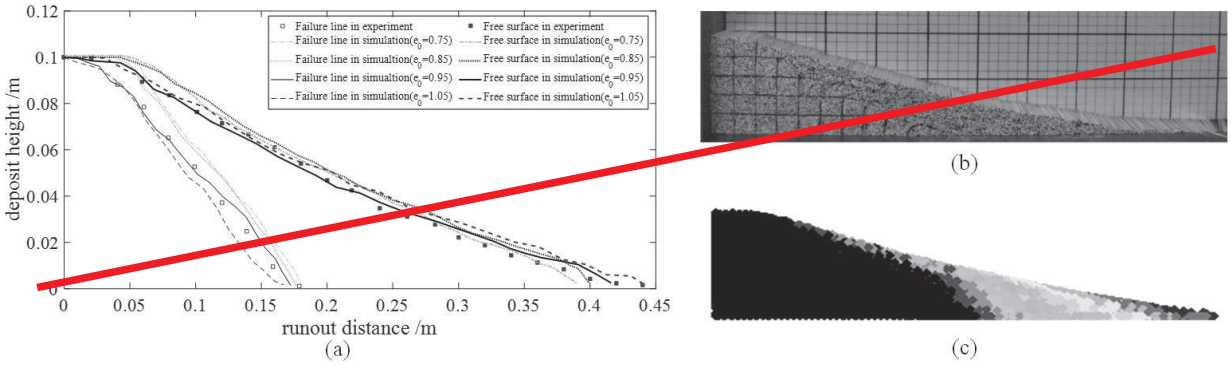
Failure line in experiment
Free surface in experiment
Failure line in simulation(e_0=0.75)
Free surface in simulation(e_0=0.75)
Failure line in simulation(e_0=0.85)
Free surface in simulation(e_0=0.85)
Failure line in simulation(e_0=0.95)
Free surface in simulation(e_0=0.95)
Failure line in simulation(e_0=1.05)
Free surface in simulation(e_0=1.05)
deposit height /m
runout distance /m
(a)
(b)
(c)

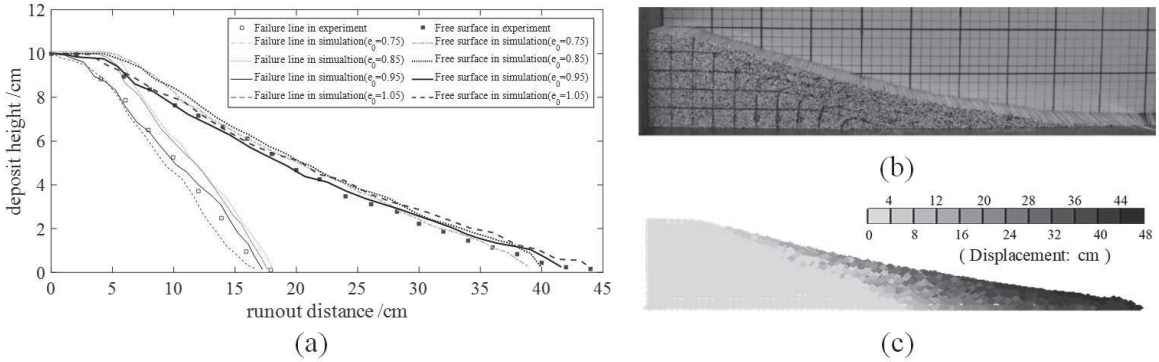
Failure line in experiment
Free surface in experiment
Failure line in simulation(e_0=0.75)
Free surface in simulation(e_0=0.75)
Failure line in simulation(e_0=0.85)
Free surface in simulation(e_0=0.85)
Failure line in simulation(e_0=0.95)
Free surface in simulation(e_0=0.95)
Failure line in simulation(e_0=1.05)
Free surface in simulation(e_0=1.05)
deposit height /cm
runout distance /cm
(a)
(b)
4 12 20 28 36 44
0 8 16 24 32 40 48
(Displacement: cm)
(c)

Figure 6

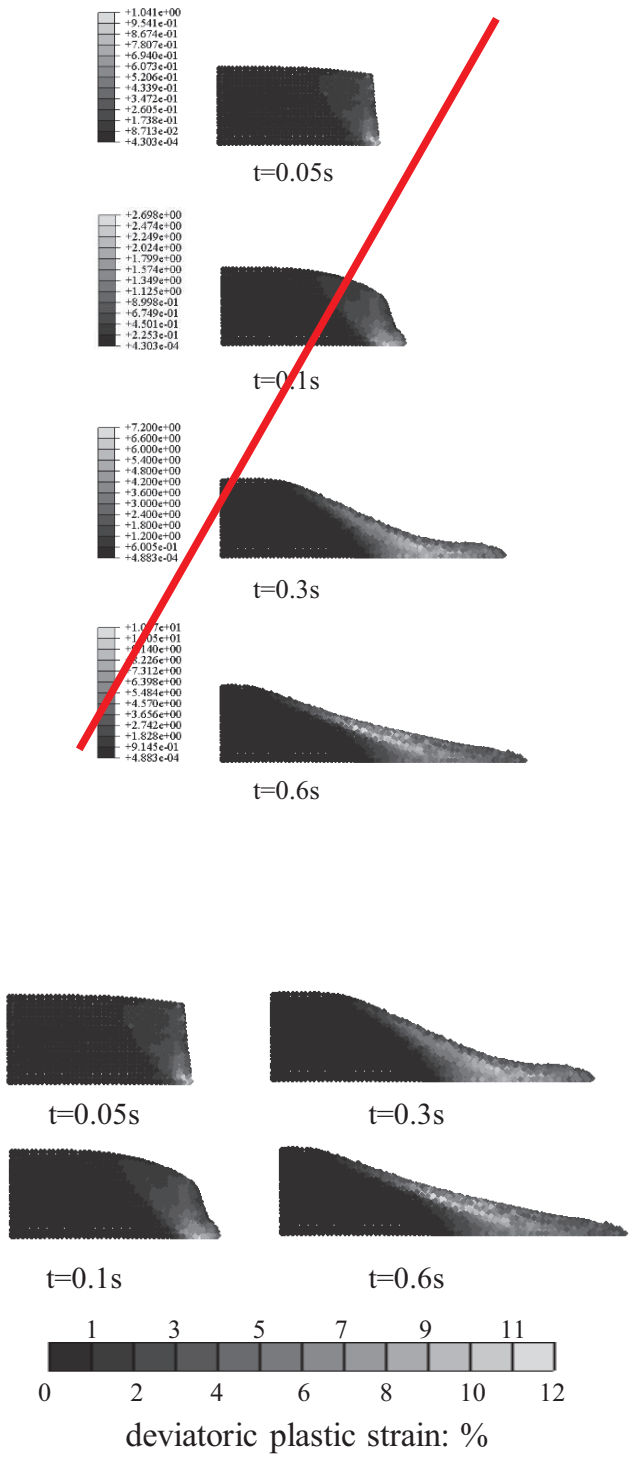

Figure 7

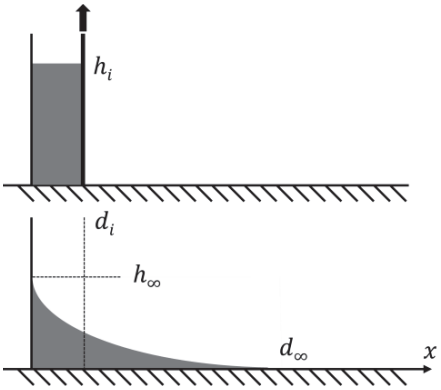

Figure 8

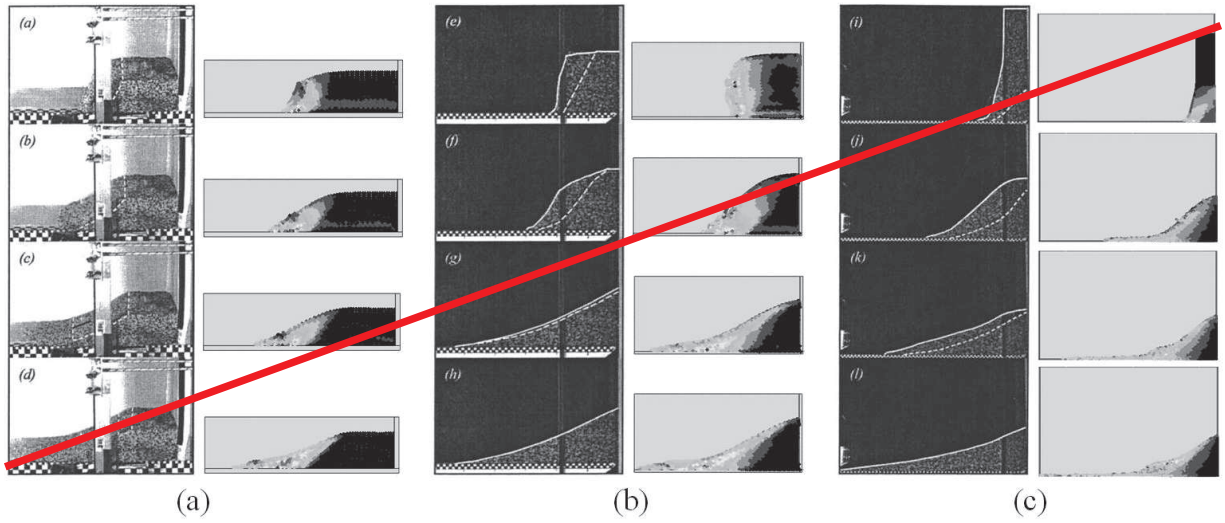

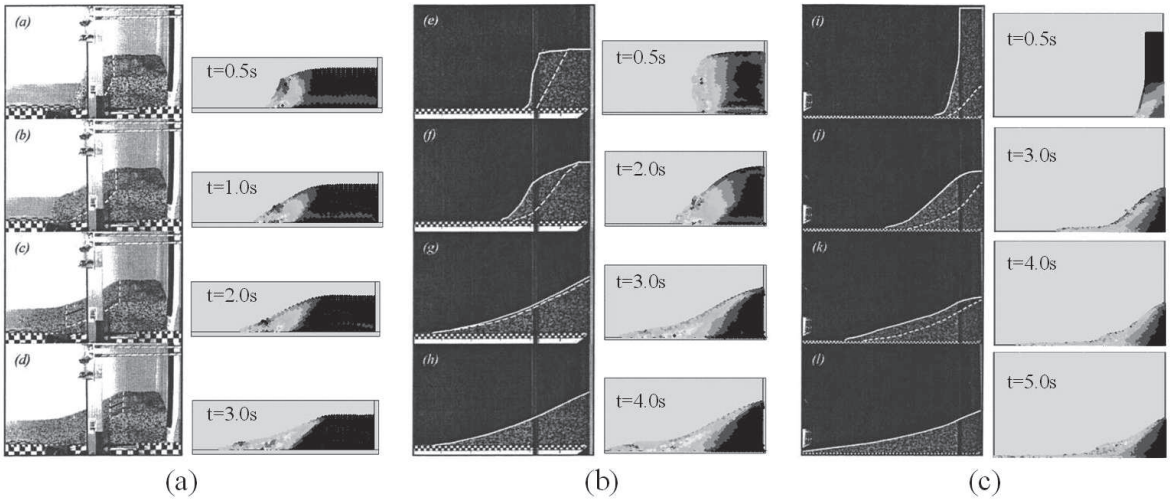

Figure 9

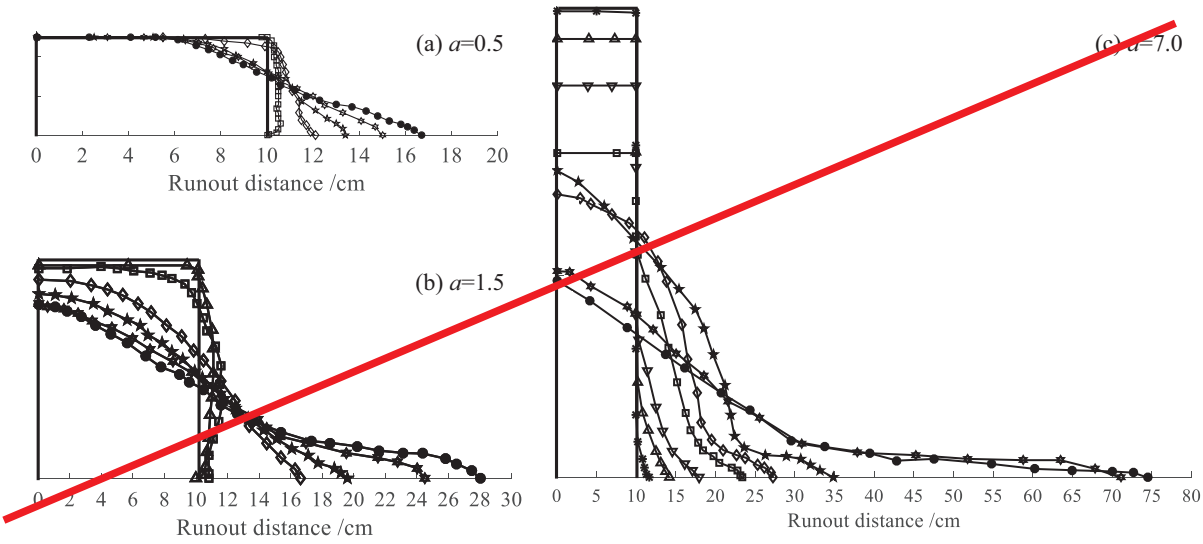

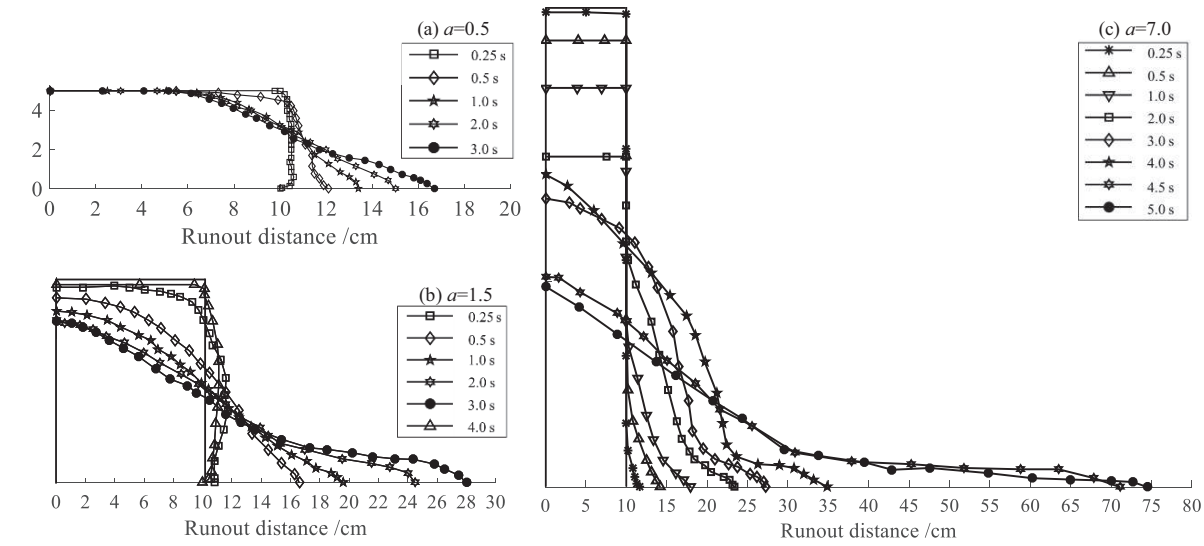

Figure 10

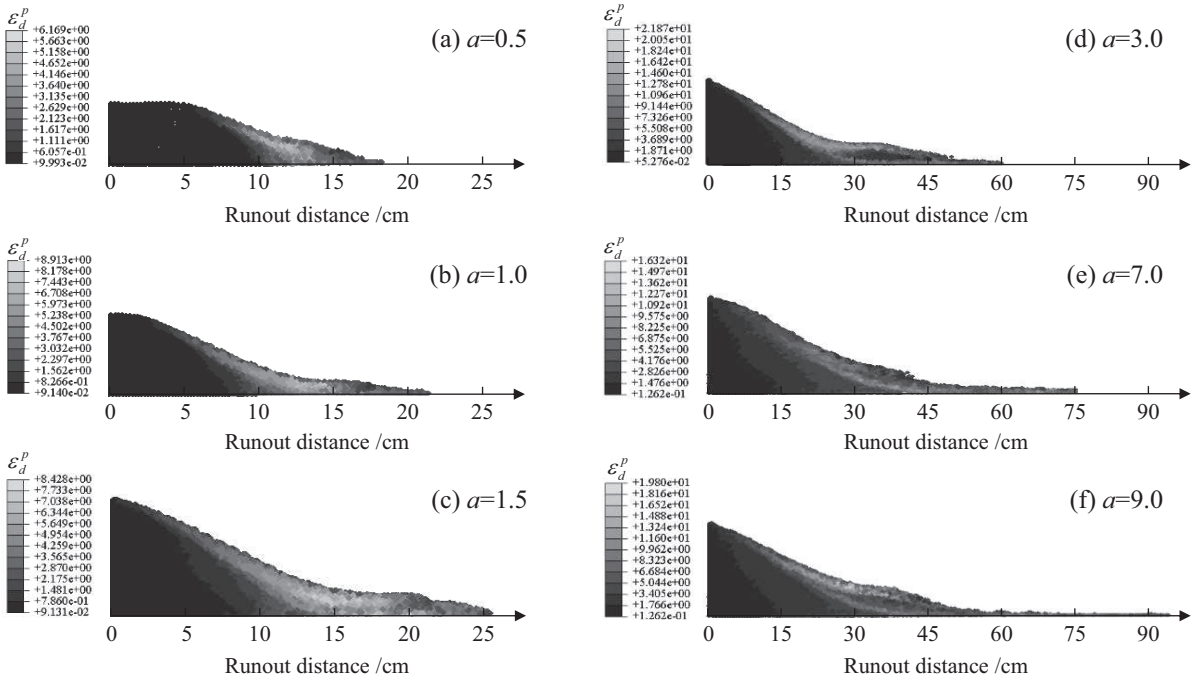

Figure 11

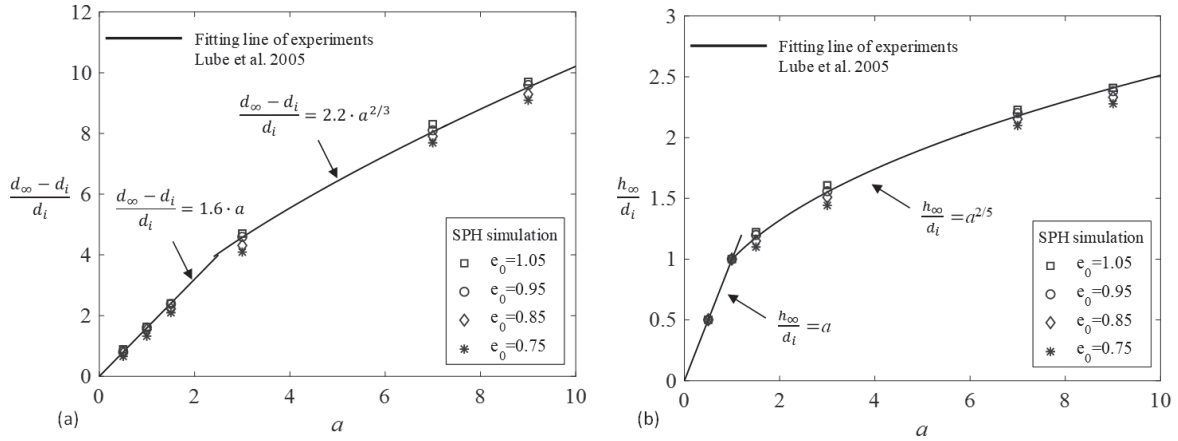

Figure 12

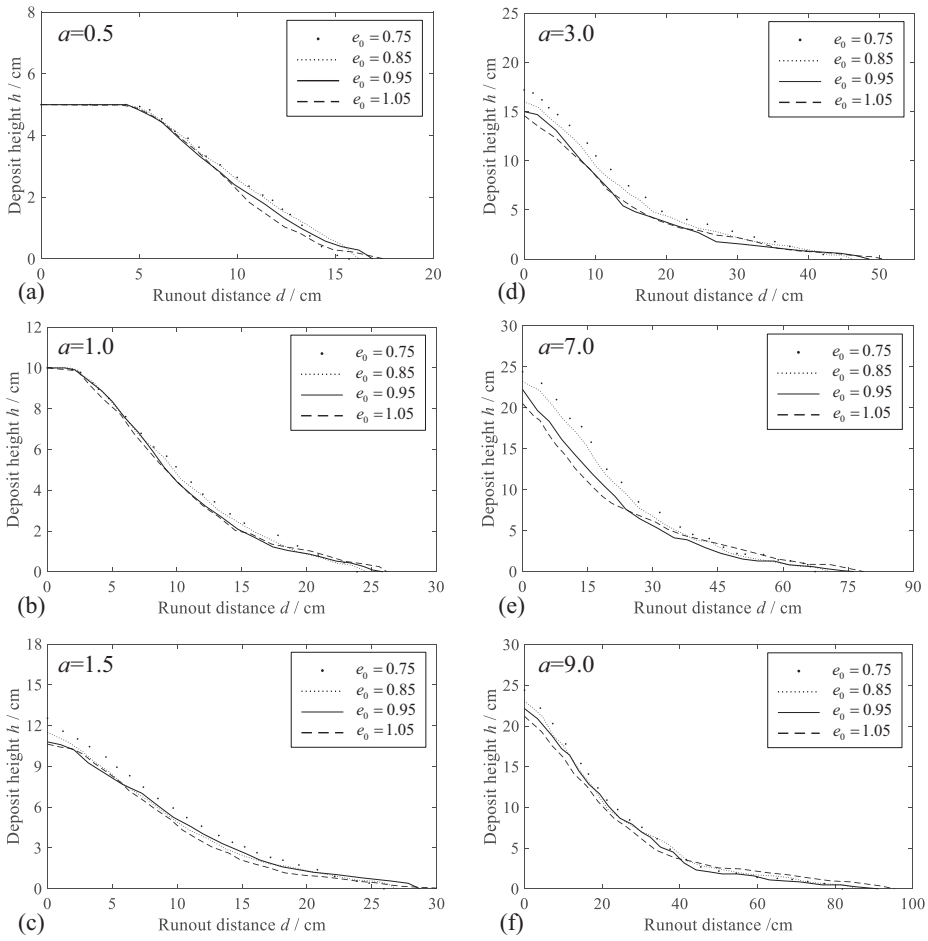
a=0.5
a=1.0
a=1.5
a=3.0
a=7.0
a=9.0
$e_0 = 0.75$
$e_0 = 0.85$
$e_0 = 0.95$
$e_0 = 1.05$
Deposit height h / cm
Runout distance d / cm
Runout distance /cm
(a)
(b)
(c)
(d)
(e)
(f)

Figure 13

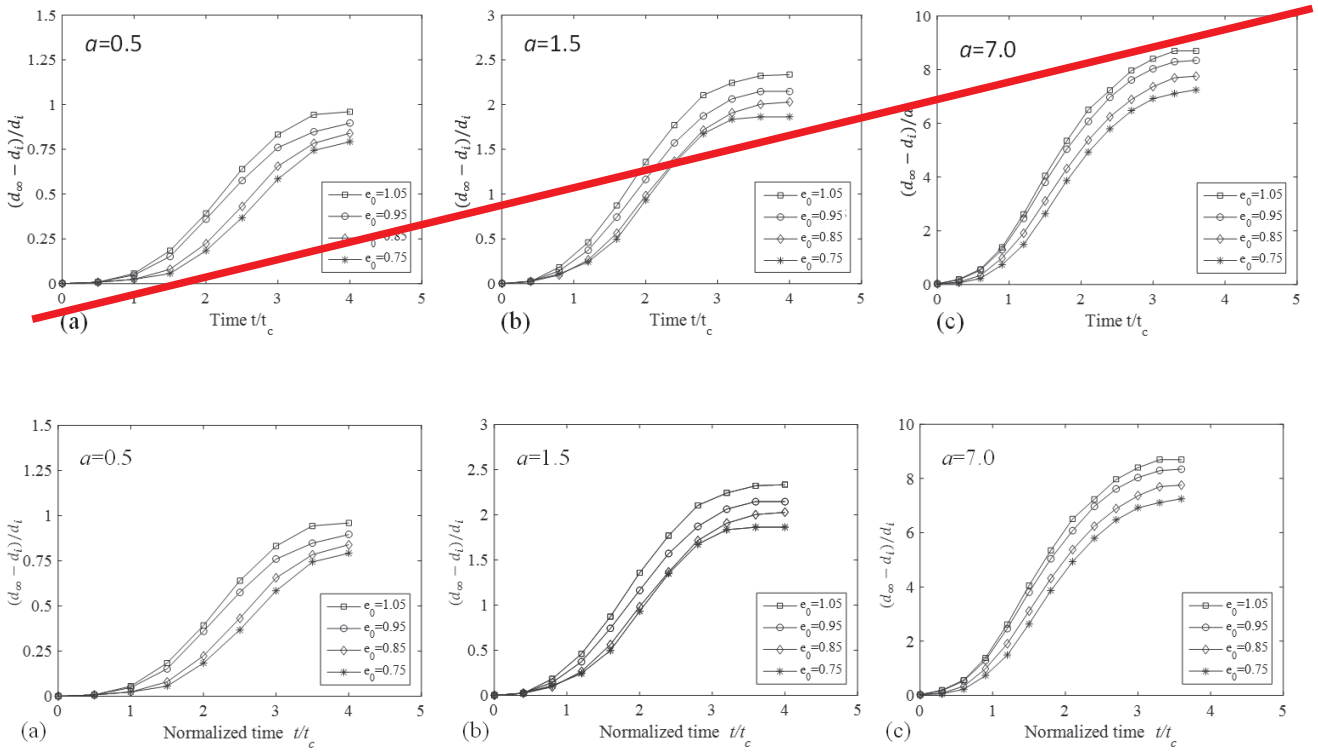
a=0.5
a=1.5
a=7.0
$(d_\infty - d_i)/d_i$
Time t/t$_c$
Normalized time t/t_c
(a)
(b)
(c)
e$_0$=1.05
e$_0$=0.95
e$_0$=0.85
e$_0$=0.75

Figure 14

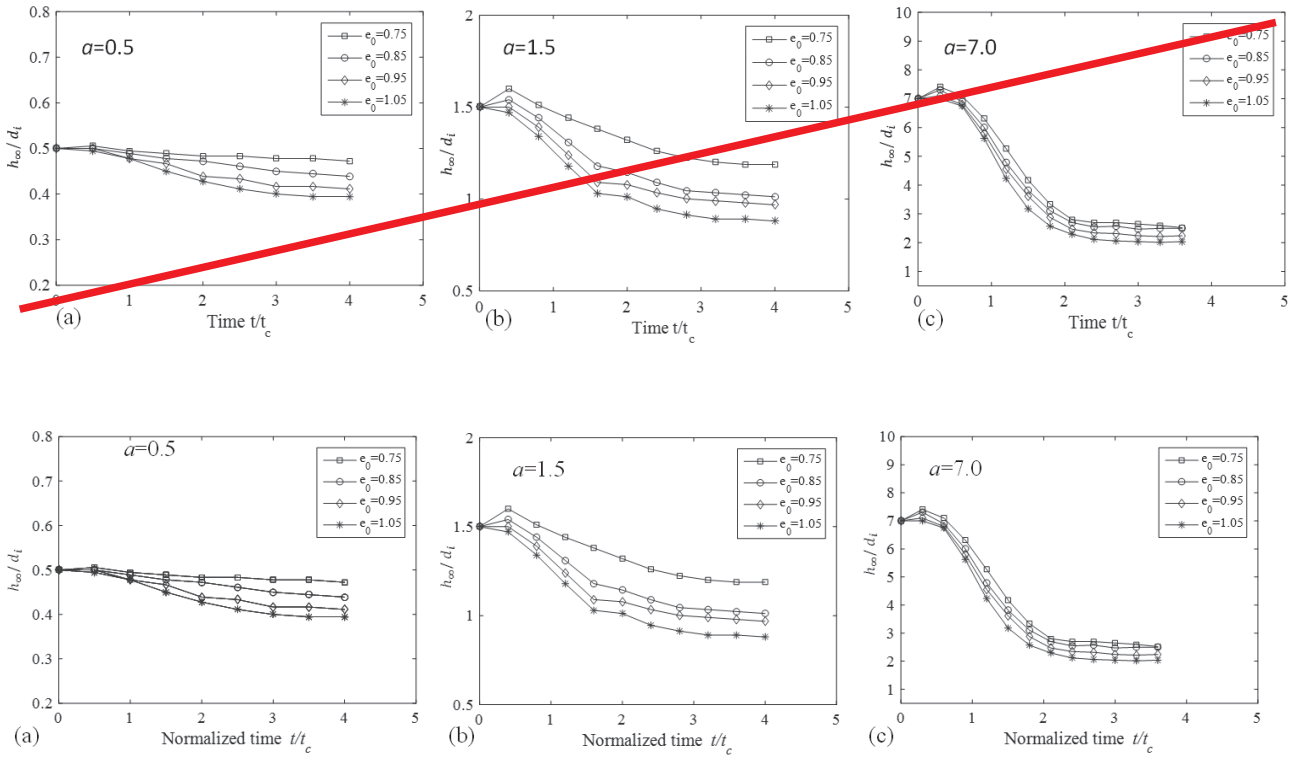
a=0.5
a=1.5
a=7.0
e0=0.75
e0=0.85
e0=0.95
e0=1.05
h∞/ di
Time t/tc
(a)
(b)
(c)
Normalized time t/tc